

Kinetics of Diesel Nanoparticle Oxidation

KELLY J. HIGGINS,[†] HEEJUNG JUNG,[‡]
DAVID B. KITTELSON,[‡]
JEFFREY T. ROBERTS,^{*,†} AND
MICHAEL R. ZACHARIAH^{*,†,‡}

Department of Chemistry, University of Minnesota,
207 Pleasant Street SE, Minneapolis, Minnesota 55455,
and Department of Mechanical Engineering,
University of Minnesota, 111 Church Street SE,
Minneapolis, Minnesota 55455

The technique of high-temperature oxidation tandem differential mobility analysis has been applied to the study of diesel nanoparticle oxidation. The oxidation rates in air of diesel nanoparticles sampled directly from the exhaust stream of a medium-duty diesel engine were measured over the temperature range of 800–1140 °C using online aerosol techniques. Three particle sizes (40, 90, and 130 nm mobility diameter) generated under engine load conditions of 10, 50, and 75% were investigated. The results show significant differences in the behavior of the 10% load particles as compared to the 50 and 75% load particles. The 10% load particles show greater size decrease at temperatures below 500 °C and significant size decrease at temperatures between 500 and 1000 °C in a non-oxidative environment, indicating release of adsorbed volatile material or thermally induced rearrangement of the agglomerate structure. Activation energies determined are 114, 109, and 108 kJ mol⁻¹ for the 10, 50, and 75% load particles, respectively. These activation energies are lower than for flame soot (Higgins et al. *J. Phys. Chem. A* **2002**, *106*, 96), but the preexponential factors are lower by 3 orders of magnitude, and the overall oxidation rates are slower by up to a factor of 4 over the temperature range studied. Possible reasons for the differences are discussed in the text.

Introduction

Particulate emission from diesel engines is currently a topic of great concern from both pollution and public health standpoints. The United States EPA is set to introduce strict new regulations on diesel particle emissions, and a number of other countries are considering regulatory action. Although specific output depends on operating conditions, the largest single component of diesel particle emissions is carbonaceous soot produced by the incomplete combustion of diesel fuel. A great deal of research effort is currently being devoted to reducing the amount of particulate matter produced by diesel engines. These efforts include making the combustion process more efficient inside the combustion chamber as well as removing particles from the exhaust stream. Past

efforts have involved increasing the in-cylinder oxidation rate of soot particles through the use of catalysts added to the fuel, while most current efforts involve the trapping of particles in a filter followed by catalytic oxidation of the trapped soot particles to regenerate the filter. For these reasons, detailed kinetic measurements of the particle oxidation process at temperatures relevant to in-cylinder or exhaust after-treatment conditions are desirable.

The kinetics of soot oxidation has been studied extensively in the past using a variety of materials and techniques (1). Early work used carbon filaments (2) and carbon or graphite rods (3, 4), while later work used various carbon blacks (5, 6) or soot generated in a flame or engine (6–13). Most previous studies that have utilized flame- or engine-generated soot have relied on collecting and immobilizing the soot (6–11) or light scattering or absorption within a flame environment (12). Recently, we developed a method to study the kinetics of soot oxidation using on-line aerosol techniques on freshly generated, size-selected soot particles (14). This method has several advantages over previous methods. It utilizes freshly generated soot so possible effects of aging on the reactivity of the soot are eliminated. Aerosol techniques eliminate the effects of reactant diffusion and transport encountered if the soot is collected and immobilized. They also allow precise control of the gas-phase environment, which is not possible within the complex chemical environment of a flame. Size selecting the soot particles allows size-dependent effects on the reactivity to be examined.

While the oxidation kinetics of soot and soot surrogates have been extensively studied, less well studied are the oxidation kinetics of diesel particles. Previous studies have again mostly utilized collection and off-line analysis of diesel particle oxidation (6–9), while some have explored the use of various carbon blacks as diesel particle surrogates (6, 11). A recent study by Song et al. (13) used diesel particles freshly generated in a diesel engine and then burned in a methane flame to study the oxidation kinetics. While the investigation found the oxidation rate dependent on O₂ partial pressure, it is unclear what role other oxidants, such as OH, present in the flame environment played in the particle oxidation. One significant limitation evident in the previous studies of diesel particle oxidation, with the exception of the work by Song et al. (13), is the limited range of temperatures investigated. In many cases, the temperature is limited by the onset of particle ignition due to excessive heating of the immobilized bed, and the maximum temperature reported for relevant previous studies is 700 °C. Aerosol techniques are not limited by particle ignition because of efficient thermalization of the particles by the carrier gas.

Diesel particles can differ significantly from proposed surrogates such as soot particles generated in a flame using hydrocarbon fuels or manufactured carbon blacks (15). Elements such as sulfur, which is present in diesel fuel, and metals from lubricating oil and cylinder abrasion can be incorporated in the diesel particles and alter the chemical properties of the particles (8, 11, 16). In addition, the fundamental carbon-to-hydrogen ratio may be different in diesel particles as compared to the commonly used surrogates (15). For these reasons, studies of diesel particle oxidation should rely on particles freshly generated and sampled directly from a diesel engine into the experimental apparatus. The present study accomplishes this by utilizing our previously developed method for the study of diesel particle oxidation.

* Address correspondence to either author. (J.T.R.) telephone: (612)625-2363; fax: (612)626-7541; e-mail: roberts@chem.umn.edu. (M.R.Z.) telephone: (612)626-9081; fax: (612)625-6069; e-mail: mrz@me.umn.edu.

[†] Department of Chemistry.

[‡] Department of Mechanical Engineering.

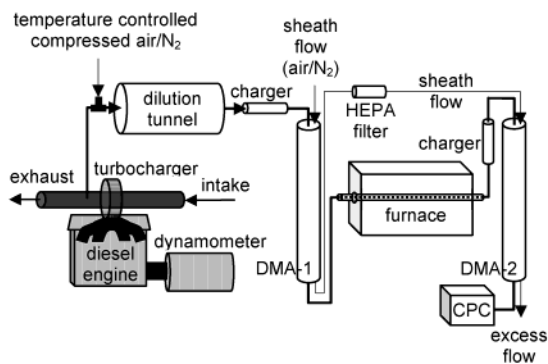


FIGURE 1. Schematic diagram of the experimental apparatus. The bold line indicates the path taken by the soot particles.

TABLE 1. Engine Conditions at 1400 rpm

load (%)	torque (Nm)	exhaust temp (°C)	air/fuel ratio (g/g)
10	40	160	101
50	200	360	37
75	300	560	27

Experimental Section

The experimental apparatus is shown schematically in Figure 1. It consists of a diesel engine from which exhaust is sampled, diluted, and then sent to a high-temperature oxidation tandem differential mobility analyzer (HTO-TDMA) for oxidation rate measurements. The engine is a medium-duty, direct injection, 4 cylinder, 4 cycle, mid-1990's turbocharged diesel engine of 4.5 L displacement with a peak power output of 125 HP (93 kW) at 2400 rpm and a peak torque output of 400 Nm at 1400 rpm. The output of the engine is coupled to a dynamometer for load control. For the current study, the engine was operated at 1400 rpm under 10% load (40 Nm), 50% load (200 Nm), and 75% load (300 Nm) conditions. Table 1 lists the operating conditions such as exhaust temperature and air-to-fuel ratio typical for each load condition. Standard EPA No. 2 on-road diesel fuel of 300–500 ppm sulfur was used, and the lubricating oil was SAE15W-40 (John Deere TY6391). Exhaust was sampled 25 cm downstream of the turbocharger exit and diluted in a two-stage, air injector, variable residence time dilution tunnel (17). Samples for the current study were taken after the first stage of dilution, which was operated with a fixed residence time at a cold flow dilution ratio of ~10:1. The first stage dilution air temperature was controlled to maintain a temperature of 32 °C at the exit from the first dilution stage.

The sampled output is then introduced to the HTO-TDMA described in detail previously (14). Briefly, in the HTO-TDMA, the sample is sent through a bipolar diffusion charger to establish a known charge distribution (18), and then a specific particle size is selected with DMA-1. The monodisperse particles then undergo oxidation in air while traveling through a quartz flow tube enclosed in a tube furnace, after which they are recharged in a bipolar diffusion charger, and the size change resulting from the high-temperature processing is measured using DMA-2. Three initial particle sizes of 40, 90, and 130 nm mobility diameter were selected to match the previous study on flame soot oxidation (14). Furnace temperature settings ranged from room temperature (25–34 °C, depending on the day) to 1100 °C. Additional experiments were performed in which air for the first dilution stage and DMA sheath flows was replaced with nitrogen (Airgas, industrial grade). These experiments were done to measure particle size decreases that were associated with non-oxidative effects, such as evaporation. Measurements

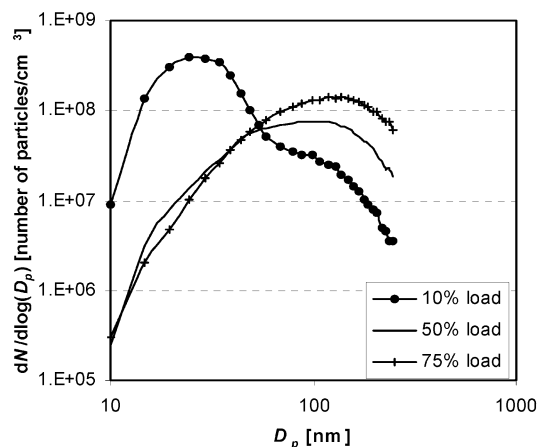


FIGURE 2. Overall diesel particle size distributions for 10, 50, and 75% engine loads, measured by bypassing DMA-1 and scanning DMA-2.

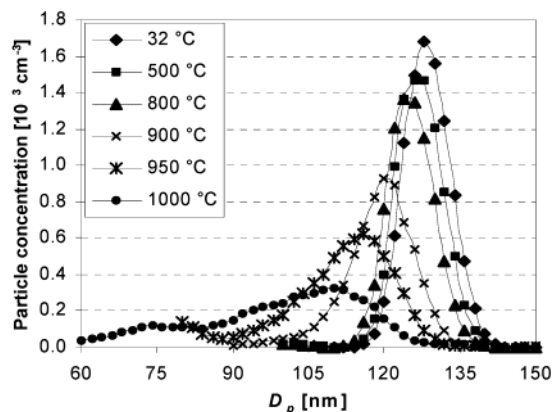


FIGURE 3. Representative TDMA data for the oxidation of particles generated under 50% engine load conditions.

of the overall size distribution of diesel particles after the first stage of dilution were made by bypassing DMA-1 and scanning DMA-2.

Results and Analysis

Figure 2 shows the results of the overall particle size distribution measurements for the three operating conditions. Note the bimodal distribution produced at 10% load, with a large number of nanoparticles in the nucleation mode, peaked at roughly 30 nm. This nucleation mode is very sensitive to the dilution conditions and is comprised mostly of volatile particles of unburned hydrocarbons and sulfates nucleated in the exhaust stream (19), with a small fraction being carbonaceous particles. The 50 and 75% load results show no or very few nucleation mode particles. Rather, there are large accumulation modes that consist entirely of carbonaceous particles formed in the combustion process.

Figure 3 shows representative HTO-TDMA data, in this case for particles of selected mobility diameter 130 nm generated under 50% load conditions. The particles shrink as the furnace temperature increases, with ΔD_p , the change in mobility diameter, equal to 1 nm at 500 °C and to 18 nm at 1000 °C. (The second peak that appears in the small size region for the 950 and 1000 °C data is due to multiple charging of the particles.) Some particle shrinkage is associated with non-oxidative processing, and some of it is due to the oxidative removal of material from the particles. Above 500 °C, most of the diameter change is due to particle oxidation. Oxidative processing can be distinguished from non-oxidative processing by comparing the HTO-TDMA scans to scans for

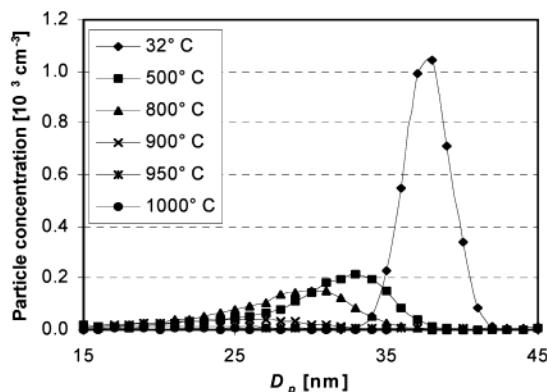


FIGURE 4. Representative TDMA data for the oxidation of particles generated under 10% engine load conditions.

which nitrogen, not air, was used as the carrier gas. From these experiments, it may be shown that virtually all of the diameter decrease at 500 °C is associated with non-oxidative processing, possibly the evaporation of volatile or semivolatile material. The non-oxidative diameter change at 1000 °C is ~3 nm, larger than that at 500 °C but only ~15% of the diameter change measured when air is used as the carrier gas. Results for other particle sizes selected at 50 and 75% load are similar.

Figure 4 shows HTO-TDMA results for 10% load particles of selected mobility diameter 40 nm. Oxidative processing is similar to that which occurs in particles generated under higher load conditions. However, low-load particles are much more subject to non-oxidative processing. Partly, this may be seen by comparing the ΔD_p values. For the 10% load particles, ΔD_p at 500 °C is ~4 nm, irrespective of the carrier gas, as compared to ~1 nm for the higher load particles. At 1000 °C, ΔD_p for the low-load particles is ~11 nm with nitrogen as the carrier gas as compared to 3 nm for the 50 and 75% load particles. The much larger non-oxidative size decrease at 500 °C is attributed to the large amount of volatile material that, in addition to forming the large peak of nucleation mode particles seen in Figure 2, condenses onto the particles in the dilution and cooling region of the sampling system. The cause of the large size decrease observed in nitrogen between 500 and 1000 °C is unclear at this point but may be due to further evaporation of low volatility adsorbates or to thermally induced rearrangement of the particle structure.

The different non-oxidative response of the low-load particles can also be seen in the greater extent to which some of the particles completely disappear, even at low furnace settings. Figure 5 plots the fractional penetration of particles leaving DMA-2 versus the furnace setting for different selected particle sizes and engine loads. Fractional penetration is defined as the ratio of the integrated area of a peak at a specified furnace setting to that when the furnace is set to room temperature. Above room temperature, the fractional penetration is expected to be less than unity, because some particles will be lost to thermophoresis. However, thermophoretic losses should be the same for particle streams of the same size experiencing the same furnace temperatures. From Figure 5, it can be seen that this is not the case. For instance, the fractional penetration of 40 nm, 10% load particles at 500 °C is 0.45 as compared to ~0.7 for the 50 and 75% load particles. Also evident is a more modest effect associated with particle size, with smaller particles more subject to complete disappearance. This effect is seen at all engine loads, although much of the higher load data are not reported in Figure 5. For the 50 and 75% load particles at a furnace setting of 500 °C, the fractional penetration is ~0.7 at a selected mobility diameter of 40 nm and ~0.9 at selected

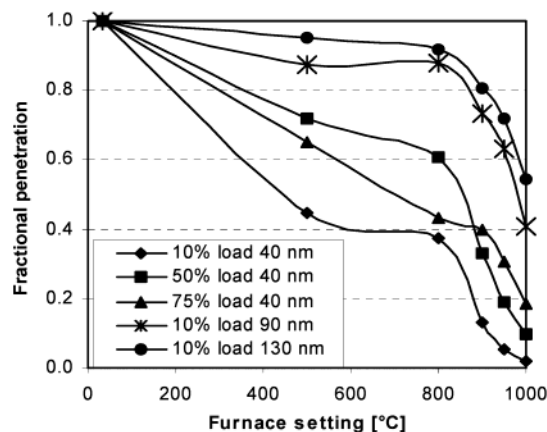


FIGURE 5. Particle losses, measured as fractional penetration, for several initial particle size and engine load combinations.

diameters of 90 and 130 nm. This appears to indicate that a substantial portion of the 40-nm 50 and 75% load particles can be considered nucleation mode particles. The sharp drop in total particle counts above 800 °C for all particle sizes and engine loads seen in Figure 5 is not completely understood, and a more detailed study of particle losses is required to elucidate the cause.

Analysis of the measured particle size decreases to obtain kinetic parameters follows the procedure detailed in ref 14. The size decrease rate is modeled using a modified Arrhenius expression:

$$\dot{D}_p = -A_{nm} T^{1/2} \exp\left[-\frac{E_a}{RT}\right] \quad (1)$$

where \dot{D}_p is the change in mobility diameter with respect to time, A_{nm} is an initial size-dependent preexponential factor, and E_a is a size-independent activation energy. Values of A_{nm} and E_a are determined by integrating

$$\Delta D_p = \int_0^X \frac{\dot{D}_p(x)}{u(x)} dx \quad (2)$$

where x is the horizontal position in the tube, X is the length of the tube, and u is the flow velocity, over the heated length of the flow tube and minimizing the differences between calculated and measured ΔD_p values in a nonlinear least-squares method. The dependence of the size decrease rate and flow velocity on horizontal position is a result of their dependence on temperature as seen in eq 1 and

$$u(x) = \frac{4}{3} u_m \frac{T(x)}{T_o} \quad (3)$$

where u_m is the mean flow velocity calculated from the volume flow rate and the cross-sectional area of the flow tube, and $4/3 u_m$ is the peak volumetric flow velocity assuming laminar flow.

Size decreases due to oxidation are determined relative to the size of the particles at 500 °C. In thermal-optical methods for determining the organic carbon (OC) and elemental carbon (EC) content of particle samples, such as the NIOSH (20) or IMPROVE (21) methods, it is common to observe oxidation of pyrolyzed OC at a lower temperatures. For our method, we do not expect to see this oxidation of pyrolyzed OC because we are heating in an oxidative environment; therefore, the OC will oxidize before it pyrolyzes.

Data from all furnace settings and initial particle sizes for each engine load are fit together to determine a different set of parameters for each engine load studied. Table 2 lists the

TABLE 2. Fitted Kinetic Parameters

	10%	50%	75%
E_a (kJ mol ⁻¹)	114	109	108
A_{40} (10 ⁴ nm K ^{-1/2} s ⁻¹)	8.8	3.1	2.6
A_{90} (10 ⁴ nm K ^{-1/2} s ⁻¹)	7.7	4.5	3.8
A_{130} (10 ⁴ nm K ^{-1/2} s ⁻¹)	11.2	5.4	4.8

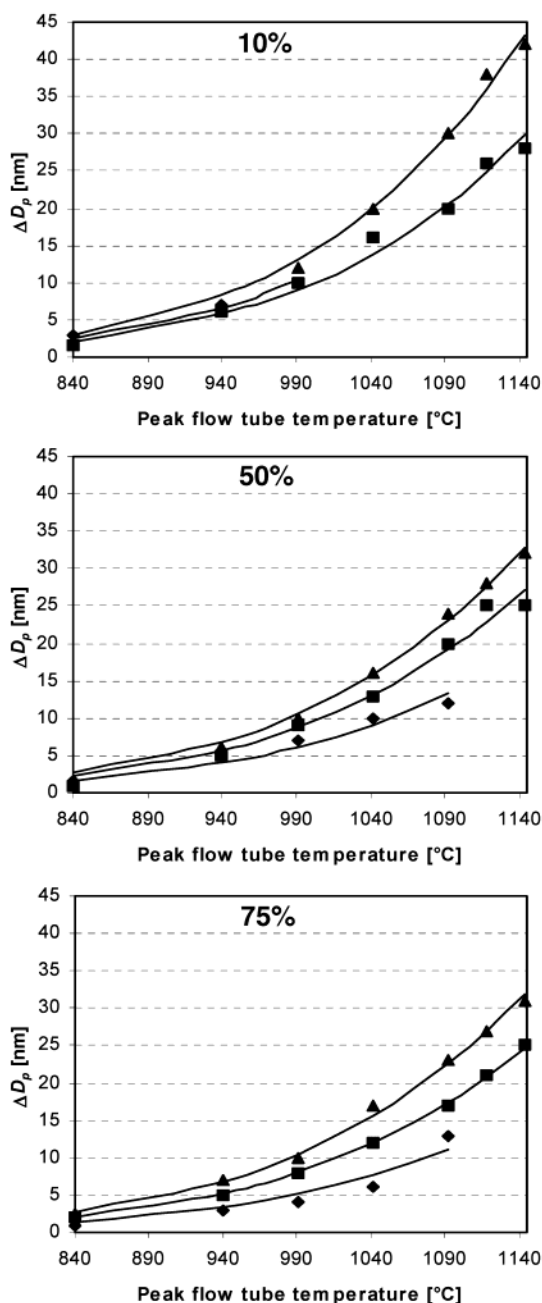


FIGURE 6. Particle size change as a function of peak flow tube temperature for particles sampled from the exhaust while the diesel was running under 10 (top), 50 (middle), and 75% (bottom) load. Initial particle sizes selected were 40 (diamonds), 90 (squares), and 130 (triangles) nm for all three engine loads. Symbols represent experimental data, and solid lines represent model results using the fitted parameters in Table 2.

fitted parameters, and Figure 6 shows graphically the experimental and calculated size reduction data. As was found for flame-generated soot particles, at 50 and 75% engine load the 130-nm particles decrease in size faster due to oxidation than the 90-nm particles, which in turn decrease faster than

TABLE 3. Preexponential Factors Adjusted for Effective Density^a

	10%	50%	75%
A'_{40} (10 ⁻² kg m ⁻² K ^{-1/2} s ⁻¹)	6.0	1.9	1.7
A'_{90} (10 ⁻² kg m ⁻² K ^{-1/2} s ⁻¹)	3.3	1.6	1.4
A'_{130} (10 ⁻² kg m ⁻² K ^{-1/2} s ⁻¹)	3.8	1.5	1.4

^a Effective density values are taken from Park et al. (22).

the 40-nm particles. The 10% load particles behave similarly except the 40-nm particles decrease faster than the 90-nm particles. Data on the 40-nm 10% particles are somewhat limited, and the size decreases of the 10% load particles include some thermal effects and not just oxidation effects. For the 75% load particles, the ratio of rates is 1:0.76:0.48; for the 50% load particles, the ratios are 1:0.81:0.59; and for the 10% load particles, the ratio is 1:0.70:0.78. The activation energy for the 50 and 75% load particles is quite similar, 109 and 108 kJ mol⁻¹, respectively, while the activation energy for the 10% load particles is 114 kJ mol⁻¹. The A_{nm} values for the 50 and 75% load particles are close to each other while for the 10% load particles they are ~2 times higher than the 50 and 75% load A_{nm} values.

The kinetic analysis presented above suggests that E_a for diesel particle oxidation is independent of initial particle size, whereas A_{nm} depends on initial size. There are several possible explanations for a preexponential factor that varies with size. For instance, the smallest particles studied in this work (<ca. 90 nm) are always in the free molecule flow regime, whereas the largest particles experience continuum or transition flow. Another explanation relates to effective particle density, which need not be independent of size for particles, like soot, that have an aggregate structure. The mass-based surface specific oxidation rate (i.e., the change in particle mass with respect to time) is related to the size reduction rate:

$$w = \frac{\rho_{eff}}{2} D_p \quad (4)$$

where w is the mass-based oxidation rate. Using eq 4, a density-adjusted preexponential factor, A'_{nm} , may be defined that is related to A_{nm} through the factor $(\rho_{eff}/2)$. Using recently measured diesel particle density data of Park et al. (22), in which they measured the mass of DMA selected particles generated using the same engine and dilution system and run under the same load conditions as the current study, it is possible to assess the effect of particle effective density. Values for A'_{nm} are listed in Table 3. The density-adjusted preexponential factors are nearly independent of initial size between 40 and 130 nm for particles generated under 50 and 75% load conditions. For these particles then, the size-dependent A_{nm} can be attributed entirely to density effects. The A'_{nm} factors do not collapse to a single value for the 10% load particles. As has already been described, these particles exhibit several unexpected properties. The origin of the size-dependent preexponential factors in 10% load particles as well as the origin of second-order effects in other particles awaits further study.

Discussion

It is informative to compare the previous results for flame soot oxidation (14) with the current results for diesel particle oxidation. Figure 7 shows the difference in size reduction rate for flame soot and diesel particles, where the diesel particle rate is up to 4 times slower than the flame soot rate over the temperature range studied. The activation energies determined for diesel particles are significantly lower than the 164 kJ mol⁻¹ activation energy determined for flame soot,

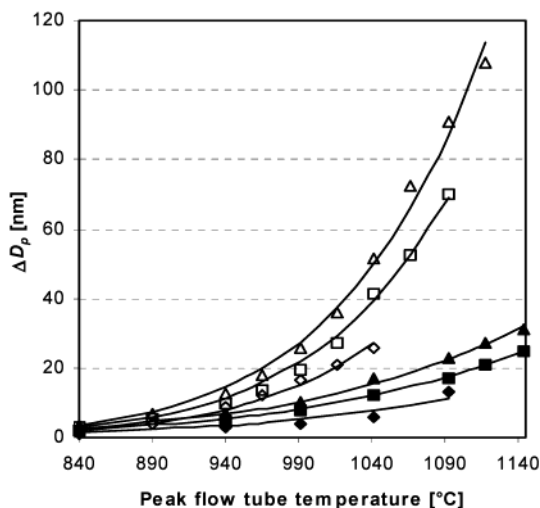


FIGURE 7. Comparison of diesel particles (solid symbols) with flame-generated soot particles (open symbols). Shown is experimental data and fitted models for 40 (diamonds), 90 (squares), and 130 (triangles) nm diesel particles from the engine at 75% load and flame soot particles of similar sizes from a previous study (14).

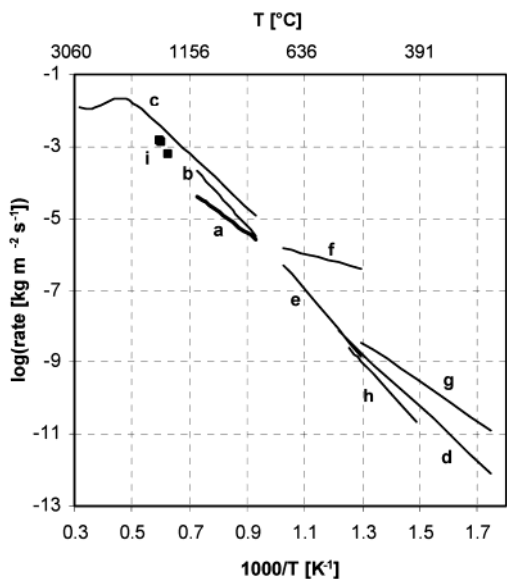


FIGURE 8. Arrhenius plot of the surface specific rate of diesel particle oxidation for the current study and for several relevant previous studies. Lines are as follows and results are presented for 21% O₂ except as indicated: (a) Current study. (b) Previous study by the authors using flame-generated soot (14). (c) Nagle and Strickland-Constable using a pyrographite rod (3). (d) Otto et al. thermogravimetric analysis (TGA) of soot collected from automobile diesel engines (9). (e) Miyamoto et al. TGA of uncatalyzed diesel soot collected from a single cylinder IDI diesel engine (7). (f) Miyamoto et al. as in line e but with Ca added to the diesel fuel to act as a soot oxidation catalyst (7). (g) Ahlström and Odenbrand flow reactor study of soot collected in the exhaust stream of Volvo diesel trucks (8). (h) Neeft et al. flow reactor study of Printex-U flame soot from Degussa AG (6). (i) Song et al. burning of diesel particles from a single cylinder diesel engine in a methane flame, 3.1% O₂ (13).

but this is offset by the preexponential factors, which are 3 orders of magnitude lower than those of the flame particles. This results in overall rates that are slower for the diesel particles than for the flame soot particles for the temperature range studied. Figure 8 presents the surface specific rate for the current study and for several relevant previous studies in an Arrhenius plot. By extrapolating to lower temperatures,

it can be seen that the rates for the diesel particles and the flame soot cross at approximately 750 °C, below which the diesel particle oxidation rate is faster than the flame soot oxidation rate. Note all but one of the previous diesel studies explored the temperature region below this point. While the fitted kinetic parameters for diesel particle oxidation are very different from those for flame-generated soot, it can be seen in Figure 8 that the overall oxidation rates are not that different, especially considering the scatter of the previous studies of diesel particle oxidation.

The study presented in Figure 8 that is most relevant to the current results is that of Miyamoto et al. (7) in which they examined the oxidation rates of “usual” diesel soot and diesel soot with an oxidation catalyst incorporated into the soot by means of a fuel additive. They found an enhanced oxidation rate in an initial rapid oxidation stage for the catalyst-laden soot as compared to the usual diesel soot over the temperature range they studied, ~500–700 °C. In the case of a calcium catalyst, the catalyst lowered the activation energy from 191 to 48 kJ mol⁻¹ but also lowered the preexponential factor by 7 orders of magnitude. This last point is left without comment or explanation in the Miyamoto et al. paper (7) but may be due to the low concentration of catalyst in the soot and the correspondingly fewer number of catalytically active sites. The effect of the lowered preexponential factor can be seen by extrapolating their data to higher temperatures. The rates for the catalyzed and uncatalyzed reactions will cross at approximately 760 °C, making the catalyzed reaction slower than the uncatalyzed reaction.

Although the Miyamoto et al. (7) results are more dramatic than the differences between the current study and the previous flame soot study, they can help explain the differences we observed. It is well-known that metals, including calcium, are found in varying quantities in diesel soot as a result of additives to the lubricating oil or to the diesel fuel itself (8, 9). In fact, previous studies of diesel particle oxidation have mentioned the possibility of oxidation rate enhancement due to the presence of inorganic impurities such as metals or metal oxides (9). The effect of such catalysts would be to lower the activation energy for oxidation, while the effect on the observed oxidation rate would depend on a number of variables such as catalyst concentration and temperature range investigated.

It appears that diesel particles may be inherently slower to oxidize than flame soot particles. If diesel soot behaved similarly to flame soot, we would expect the oxidation rate for diesel soot to be as fast or faster than the flame soot, depending on the presence of a catalyst. If the Miyamoto et al. (7) catalyzed work were extended to higher temperatures, one would expect to see a kink in the Arrhenius rate plot, with the kink coming at the crossover point between the usual diesel soot and the catalyzed diesel soot rates. The faster rate would dominate in each temperature range. The current results for diesel particles fall below the previous results for flame soot particles, indicating that the diesel particles oxidize slower.

Acknowledgments

This work was supported by the National Science Foundation through Grant CHE-0094911. K.J.H. also thanks the Camille and Henry Dreyfus Foundation for support in the form of a Postdoctoral Fellowship in Environmental Chemistry.

Literature Cited

- (1) For a recent review, see Stanmore, B. R.; Brillhac, J. F.; Gilot, P. *Carbon* **2001**, *39*, 2247.
- (2) Strickland-Constable, R. F. *Trans. Faraday Soc.* **1944**, *40*, 333 (also reviews earlier carbon oxidation studies).
- (3) Nagle, J.; Strickland-Constable, R. F. *Fifth Carbon Conference*, Vol. 1; Pergamon: Oxford, 1962; pp 154–164.

- (4) Walls, J. R.; Strickland-Constable, R. F. *Carbon* **1964**, *1*, 333.
- (5) Park, C.; Appleton, J. P. *Combust. Flame* **1973**, *20*, 369. (b) Brandt, O.; Roth, P. *J. Aerosol Sci.* **1988**, *19*, 863. (c) Brandt, O.; Roth, P. *Combust. Flame* **1989**, *77*, 69. (c) Cadman, P.; Denning, R. J. *J. Chem. Soc., Faraday Trans.* **1996**, *92*, 4159. (d) Gilot, P.; Bonnefoy, F.; Marcuccilli, F.; Prado, G. *Combust. Flame* **1993**, *95*, 87. (e) Encinar, J. M.; González, J. F.; Sabio, E.; Rodríguez, J. J. *J. Chem. Technol. Biotechnol.* **2000**, *75*, 213.
- (6) Neeft, J. P. A.; Nijhuis, T. X.; Smakman, E.; Makkee, M.; Moulijn, J. A. *Fuel* **1997**, *76*, 1129.
- (7) Miyamoto, N.; Zhixin, H.; Hideyuki, O. *SAE Tech. Pap. Ser.* **1988**, No. 881224.
- (8) Ahlström, A. F.; Odenbrand, C. U. I. *Carbon* **1989**, *3*, 475.
- (9) Otto, K.; Sieg, M. H.; Zinbo, M.; Bartosiewicz, L. *SAE Tech. Pap. Ser.* **1980**, No. 800336.
- (10) Du, Z.; Sarofim, A. F.; Longwell, J. P.; Mims, C. A. *Energy Fuels* **1991**, *5*, 214. (b) Ciambelli, P.; D'Amore, M.; Palma, V.; Vaccaro, S. *Combust. Sci. Technol.* **1996**, *121*, 67.
- (11) Yezerets, A.; Currier, N. W.; Eadler, H.; Popuri, S.; Suresh, A. *SAE Tech. Pap. Ser.* **2002**, No. 2002-01-1684.
- (12) Feugier, A. *Combust. Flame* **1972**, *19*, 249. (b) Neoh, K. G.; Howard, J. B.; Sarofim, A. F. *Particulate Carbon: Formation During Combustion*; Siegl, D. C., Smith, G. W., Eds.; Plenum: New York, 1981; pp 261–282. (c) Garo, A.; Prado, G.; Lahaye, J. *Combust. Flame* **1990**, *79*, 226. (d) Schäfer, Th.; Mauss, F.; Bockhorn, H.; Fetting, F. *Z. Naturforsch., A: Phys. Sci.* **1995**, *50*, 1009.
- (13) Song, H.; Ladommatos, N.; Zhao, H. *SAE Tech. Pap. Ser.* **2001**, No. 2001-01-3673.
- (14) Higgins, K. J.; Jung, H.; Kittelson, D. B.; Roberts, J. T.; Zachariah, M. R. *J. Phys. Chem. A* **2002**, *106*, 96.
- (15) Clague, A. D. H.; Donnet, J. B.; Wang, T. K.; Peng, J. C. M. *Carbon* **1999**, *37*, 1553.
- (16) Frey, J. W.; Corn, M. *Nature* **1967**, *216*, 615–616. (b) Hare, C. T.; Baines, T. M. *SAE Tech. Pap. Ser.* **1979**, No. 790424. (c) Berube, K. A.; Jones, T. P.; Williamson, B. J.; Winters, C.; Morgan, A. J.; Richards, R. J. *Atmos. Environ.* **1999**, *33*, 1599.
- (17) Khalek, I. A.; Kittelson, D. B. *SAE Tech. Pap. Ser.* **1999**, No. 1999-01-1142. (b) Khalek, I. A.; Kittelson, D. B.; Brear, F. *SAE Tech. Pap. Ser.* **2000**, No. 2000-01-0515.
- (18) Fuchs, N. A. *Geofis. Pura Appl.* **1963**, *56*, 185. (b) Wiedensohler, A. *J. Aerosol Sci.* **1988**, *19*, 387.
- (19) Tobias, H. J.; Beving, D. E.; Ziemann, P. J.; Sakurai, H.; Zuk, M.; McMurry, P. H.; Zarling, D.; Waytulonis, R.; Kittelson, D. B. *Environ. Sci. Technol.* **2001**, *35*, 2233.
- (20) NIOSH. *NIOSH Manual of Analytical Methods*; National Institute of Occupational Safety and Health: Cincinnati, OH, 1996.
- (21) Chow, J. C.; Watson, J. G.; Pritchett, L. C.; Pierson, W. R.; Frazier, C. A.; Purcell, R. G. *Atmos. Environ.* **1993**, *27A*, 1185.
- (22) Park, K.; Feng, C.; Kittelson, D. B.; McMurry, P. H. *Environ. Sci. Technol.* **2003**, *37*, 577–583.

Received for review September 5, 2002. Revised manuscript received January 24, 2003. Accepted February 18, 2003.

ES0261269